



An Experimental Scattering Matrix for Lunar Regolith Simulant JSC-1A at Visible Wavelengths

J. Escobar-Cerezo¹, O. Muñoz¹, F. Moreno¹, D. Guirado¹, J. C. Gómez Martín¹, J. D. Goguen², E. J. Garboczi³,
A. N. Chiaramonti³, T. Lafarge⁴, and R. A. West²

¹Instituto de Astrofísica de Andalucía, CSIC, Glorieta de la Astronomía s/n, E-18008 Granada, Spain

²Jet Propulsion Laboratory, California Institute of Technology, 4800 Oak Grove Drive, Pasadena, CA 91109, USA

³Applied Chemicals and Materials Division, Material Measurement Laboratory, National Institute of Standards and Technology, Boulder, CO, USA

⁴Statistical Engineering Division, Information Technology Laboratory, National Institute of Standards and Technology, Gaithersburg, MD, USA

Received 2017 December 20; revised 2018 January 8; accepted 2018 January 8; published 2018 March 8

Abstract

We present the experimental scattering matrix as a function of the scattering angle of the lunar soil simulant JSC-1A. The measurements were performed at 488, 520, and 647 nm, covering the range of scattering angles from 3° to 177°. The effect of sub-micron-sized particles on the measured phase function and degree of linear polarization has been studied. After removing particles smaller than a 1 μm radius, the forward-scattering peak becomes steeper. Furthermore, the maximum of the degree of linear polarization increases, moving toward smaller scattering angles. Interestingly, the negative branch in the backward direction disappears as the small particles are removed from the sample. Because multiple scattering calculations with polarization included require single scattering matrices throughout the scattering range (from 0° to 180°), we computed the corresponding synthetic scattering matrix through an extrapolation method, considering theoretical boundary conditions. From the extrapolated results, the asymmetry parameter g and the back-scattering linear depolarization factor δ_L were computed.

Key words: Moon – polarization – scattering

1. Introduction

The Moon is one of the most studied celestial bodies in astronomy. In this work we are interested in the polarimetric point of view of the object. The first polarimetric studies of the Moon surface date back to Lyot (1929). More recently, there has been an increased interest in polarimetric measurements since the work of Sterzik et al. (2012), who presented a new method for detecting spectropolarimetric biosignatures in earth-like exoplanets. In that paper, the Moon surface was used as a mirror to extract biosignatures from the Earth's spectrum. In order to improve the accuracy of this method, the background signal produced by lunar regolith has to be characterized with precision to subtract it from the spectrum.

The *Apollo* missions brought back 382 kilograms of lunar samples between 1969 and 1972. In addition, some 300 grams of samples were returned from the Moon by *Luna*'s automated missions. Due to the limited amount of lunar samples available to study, lunar simulants were developed to cover that need. In the early 1990s, a mare lunar regolith simulant designated JSC-1 (Johnson Space Center-1, McKay et al. 1994) was produced to support NASA's future lunar surface missions. This simulant was created to resemble as much as possible the composition and size distribution of lunar soil 14163 from the Apollo 14 mission. When this simulant ran out, NASA ordered a new simulant called JSC-1A, matching the JSC-1 simulant as closely as possible. This simulant has been studied from various points of view, but to our knowledge, its scattering matrix has never been measured.

In this work, we present the experimental scattering matrices as functions of the scattering angle of the JSC-1A lunar simulant at three visible wavelengths (488, 520, and 647 nm). These measurements were performed at the IAA COsmic DUSt LABoratory (IAA-CODULAB) located at the Instituto de

Astrofísica de Andalucía (Muñoz et al. 2010). The experimental apparatus is presented in Section 2. A description of the physical properties of the JSC-1A samples is presented in Section 3. The lack of measurements at very small and very large scattering angles (0°–3° and 177°–180°) limits the applicability of the measured scattering matrices for multiple scattering calculations. Therefore, we extrapolate the experimental scattering matrices to cover the entire 0°–180° angle range. The extrapolation of the components of the scattering matrix F was performed following the procedure presented by Liu et al. (2003) for the phase function and Muñoz et al. (2006) for the rest of the scattering elements. The asymmetry parameter g and the back-scattering linear depolarization factor δ_L (180°) were calculated from these extrapolated matrices. All these results are presented in Section 4. Conclusions are drawn in Section 5.

2. Experimental Apparatus

In this section, we give a brief description of the IAA-CODULAB apparatus. A detailed description of the experimental setup, including the calibration process and data acquisition, is presented in Muñoz et al. (2010). All published results are freely available at the Amsterdam–Granada Light Scattering Database (www.iaa.es/scattering).

We use an Argon–Krypton laser that is tunable to five different wavelengths in the visible range. In this work, we present the results at 488, 520, and 647 nm, as these wavelengths are sufficiently separated to obtain differences in the results, if they exist. The laser beam passes through an integrated polarizer and an electro-optic modulator, which in combination with lock-in amplifiers and an oscillator allows us to increase the accuracy of the measurements as well as determine several elements of the scattering matrix

Table 1

Composition in Mass Percentage (mass %) of the Major Constituents of the JSC-1A Lunar Simulant Compared with the *Apollo 14* Sample 14163

Constituent Oxides	<i>Apollo 14</i> sample 14163 (Papike et al. 1982)	JSC-1A (Ray et al. 2010)
SiO ₂	47.3%	45.7%
Al ₂ O ₃	17.8%	16.2%
CaO	11.4%	10.0%
FeO	10.5%	...
Fe ₂ O ₃	...	12.4%
MgO	9.6%	8.7%
TiO ₂	1.6%	1.9%
Na ₂ O	0.70%	3.2%
K ₂ O	0.55%	0.8%
MnO	0.135%	0.2%

simultaneously. The laser beam is scattered by a cloud of particles produced by an aerosol generator. Two photomultipliers located in a one-meter ring collect the signal. One of them, the monitor, is located in a fixed position to correct for fluctuations of the jet stream, while the other acts as a detector, moving from 3° to 177°. Two additional optical elements, a quarter-wave plate and an analyzer, are optionally placed in the detector photomultiplier. Using five different configurations of these optical elements, we measure the 4 × 4 scattering matrix, which has only six independent real elements when assuming mirror symmetry and randomly oriented particles in the sample (Hovenier et al. 2004):

$$\mathbf{F} = \begin{pmatrix} F_{11} & F_{12} & 0 & 0 \\ F_{12} & F_{22} & 0 & 0 \\ 0 & 0 & F_{33} & F_{34} \\ 0 & 0 & -F_{34} & F_{44} \end{pmatrix}. \quad (1)$$

The scattering matrix elements depend on the wavelength λ and on the particle size, shape distribution, and complex refractive index of the particles. The elements also depend on the scattering angle θ , which is the angle defined by the directions of the incident and scattered beams. All scattering elements $F_{ij}(\theta)$ are normalized to $F_{11}(\theta)$, except $F_{11}(\theta)$ itself, which is normalized to unity at 30°. The $F_{11}(\theta)$ element normalized in this way is called the phase function in this work. The $-F_{12}(\theta)/F_{11}(\theta)$ ratio is equivalent to the degree of linear polarization for unpolarized incident light.

From the $F_{22}(\theta)/F_{11}(\theta)$ ratio, we can compute the linear depolarization factor at back-scattering δ_L according to the equation (Mishchenko et al. 2002):

$$\delta_L = \frac{F_{11}(180^\circ) - F_{22}(180^\circ)}{F_{11}(180^\circ) + F_{22}(180^\circ)}. \quad (2)$$

The validity of the measurements has been tested by comparing spherical water droplet measurements with Lorenz–Mie computations for homogeneous spherical particles (Muñoz et al. 2010). Moreover, special tests have been carried out to test that our measurements are performed under single scattering conditions (Muñoz et al. 2011). Furthermore, we checked that the measured scattering matrices fulfilled the Cloude coherence matrix test within the experimental errors at all measured scattering angles (Hovenier et al. 1986).

3. Physical Properties of JSC-1A Lunar Simulant.

As mentioned, the JSC-1A mare regolith simulant was produced to match the *Apollo 14* sample 14163. In Table 1, we present a composition comparison between simulant JSC-1A and the *Apollo 14* sample 14163. The JSC-1A material was mined from a commercial cinder quarry at Merriam Crater (35°20' N, 111°17' W), a volcanic cinder cone located in the San Francisco volcano field near Flagstaff, Arizona. No chemical processing was performed on the simulant.

3.1. Size Characterization

The original mined material from the cinder quarry was milled and sieved to approximate the finer component of lunar regolith, where an important percentage of grain sizes are below 20 μm . Before using the JSC-1A in our light-scattering experiment, we removed the large grains using a sieve with a 140 μm grid width to avoid clogging the aerosol generator. The size distribution was then measured with a commercial particle sizer. This instrument measures the phase function of the sample at a wavelength of 632.8 nm at certain scattering angles, with special attention paid to the forward-scattering peak. The angular patterns obtained for the phase function are compared to those simulated by the instrument software in order to retrieve the volume distribution that best fits the data. These simulations use either Lorenz–Mie (Mie 1908) or Fraunhofer diffraction theory (van de Hulst 1957) under the assumption of spherical particles to obtain numerical results. As these two methods are usually used by the astronomy community, we make available results from both. The Fraunhofer diffraction theory states that the diffraction pattern depends on the shape and size of the particle, but is independent of its composition and the nature of its surface. Because of this, the Fraunhofer approach does not require the refractive index as input to compute the volume distribution, but puts restrictions on the size of the particles, since it is only applicable to particles larger than the wavelength of the incident light. In the Lorenz–Mie calculations, we used $m = 1.65 + i0.003$ as the complex refractive index (Goguen et al. 2010). From the estimated volume distribution, we compute the number distribution of the sample $n(r)$ such that $n(r)dr$ is the relative number of spheres per unit volume in the size range r and $r + dr$. The values of the effective radius r_{eff} and effective variance v_{eff} are computed according to the following equations (Hansen & Travis 1974):

$$r_{\text{eff}} = \frac{\int_0^\infty r \pi r^2 n(r) dr}{\int_0^\infty \pi r^2 n(r) dr}, \quad (3)$$

$$v_{\text{eff}} = \frac{\int_0^\infty (r - r_{\text{eff}})^2 \pi r^2 n(r) dr}{r_{\text{eff}}^2 \int_0^\infty \pi r^2 n(r) dr}. \quad (4)$$

In Table 2, we present the resulting values for our JSC-1A sample.

As mentioned, during the experiment, the cloud of particles is located in a jet stream produced by an aerosol generator. In this way a sample container is not needed. This is very convenient because the container walls would produce reflections or stray light, thus decreasing the accuracy of the measurements and limiting the angular range. A disadvantage of this method is that we need a continuous flow of particles during the measurements, requiring a sufficient sample size. The sample has to be discarded after being blown through the

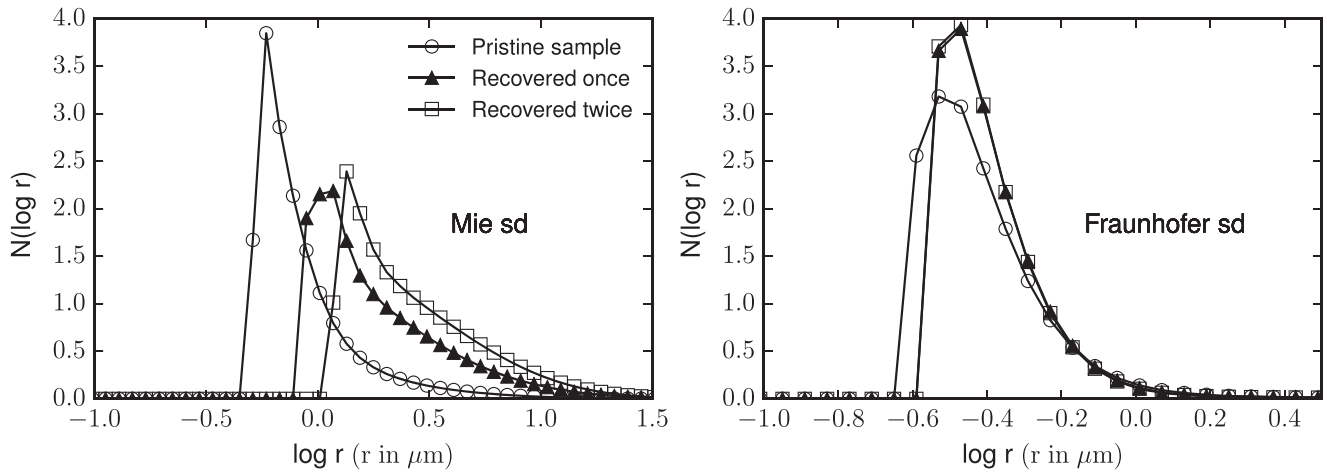


Figure 1. Number distribution $N(\log r)$ vs. $\log r$ of the pristine lunar simulant JSC-1A (circles) and the same samples after recovering once from the collecting system (triangles) and after two recoveries (squares). Retrievals based on the Mie and Fraunhofer theories are presented in the left and right panels, respectively. The refractive index used in the Mie light-scattering model is $m = 1.65 + i0.003$.

Table 2

Size Distribution Parameters r_{eff} and v_{eff} for the Pristine Sample, the Sample after Recovering Once, and Twice

Sample	Mie		Fraunhofer	
	$r_{\text{eff}} (\mu\text{m})$	v_{eff}	$r_{\text{eff}} (\mu\text{m})$	v_{eff}
Pristine	15.85	1.28	10.50	1.69
Recovered once	20.63	1.06	13.80	1.42
Recovered twice	21.86	1.05	14.67	1.45

Note. The effective radius and variance based on the Mie and Fraunhofer theories are presented in the second and third columns, respectively. For the Mie model, the refractive index used was $m = 1.65 + i0.003$ (Goguen et al. 2010).

scattering volume. In an attempt to reduce this problem, we have used a dedicated pump in order to recover the JSC-1A sample and re-use it in subsequent measurements. To check how this recycling process changes the size distribution of the sample we have performed the following test: 17 g of the bulk JSC-1A sample were recycled twice. After one recovery cycle, the mass-loss was 1.6 g, 9.4% of the original mass. After the second recovery, the loss was significantly smaller, being 0.4 g, 2.6% of the 15.4 g of the first recovered material. The size distribution of the recycled sample was measured after the first and second recoveries. The r_{eff} of the sample after the first recovery changed from 15.85 to 20.62 μm , an increase of 30%. After the second recovery, the r_{eff} value was 21.86 μm , an increase of 6% from 20.62 μm . Therefore, during the recovery process a high percentage of the small particle fraction is lost. This effect tends to saturate after the first recovery. With regard to the v_{eff} , this value varies from 1.28 for the pristine sample to 1.06 for the sample recovered once, and 1.05 for the sample recovered twice. The size distribution becomes narrower, but again this effect saturates. In Figure 1 and Table 2, we show a comparison between the number size distributions as function of $\log r$, $N(\log r)$, where $N(\log r)d \log r$ can be defined as the relative number of spheres per unit volume in the size range $\log r$ and $\log r + d \log r$. In Figure 2 we also present $S(\log r)$, which can be defined as the relative contribution to the total surface area of projected-surface-area-equivalent spheres of radius r as a function of $\log r$. As the area under the curve is

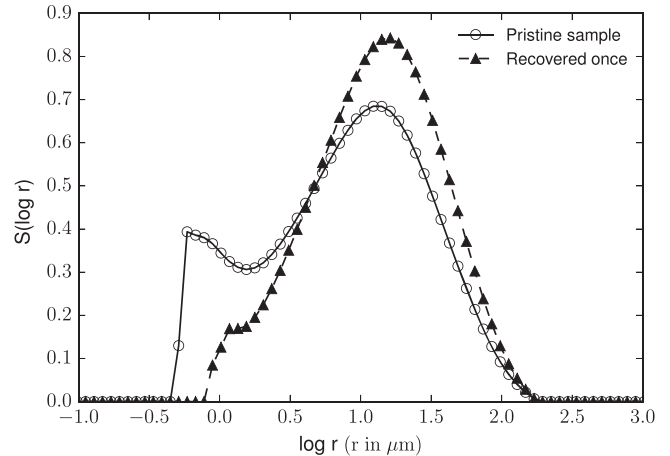


Figure 2. Projected-surface-area distribution $S(\log r)$ vs. size logarithm $\log r$ of the pristine lunar simulant JSC-1A (circles) and the same sample after recovering once from the collecting system (triangles). The Mie light-scattering model has been used to compute the size distribution with a refractive index of $m = 1.65 + i0.003$ (Goguen et al. 2010). The cut slope seen for small sizes is an artifact produced by the data retrieved from the commercial particle sizer.

normalized to unity, we observe that the recovered sample has lost the contribution of the small particles to the size distribution.

3.2. Shape Characterization

A deep analysis of the JSC-1A particle shape was presented in Garboczi (2011), where X-ray computed tomography (X-ray CT) was used to characterize the simulant. In this work, we use the same techniques to describe our sample.

In Figure 3, we show X-ray CT images qualitatively showing the shape variation in the JSC-1A lunar simulant. To prepare samples, the particles of interest were mixed with epoxy and the mixture was pulled into a narrow (3 mm diameter) plastic tube. Pieces of the tube were cut and used in the upright position as samples in one of two X-ray microCT instruments. For the image in Figure 3(c), the epoxy-particle mixture was dripped on the outside of the same tube to give a thinner sample. The thinner sample gave better images at this very high resolution than the regular samples.

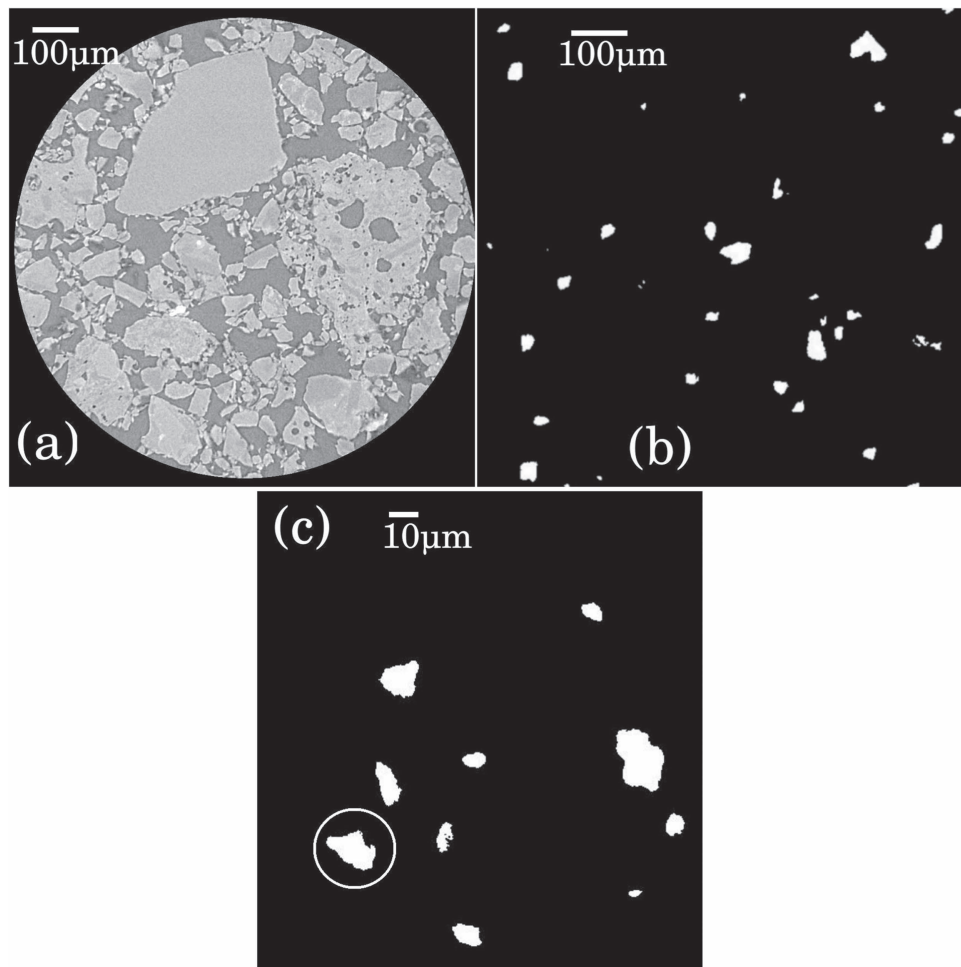


Figure 3. X-ray CT images of the JSC-1A sample. The particles were mixed with epoxy and introduced in a 3 mm diameter tube before cutting into slices. Panel (a) depicts the bulk sample, as no sieving was performed. Panel (b) shows particles in the size range of 20–75 μm after removing larger and smaller particles through sieving. Panel (c) shows the same population as (b), but with larger magnification.

Figure 3(a) is approximately 1.04 mm in width. Note the air bubbles in some of the particles. Since JSC-1A has a volcanic origin, these must be the remnants of air bubbles that were entrained during the original lava flow. The large particle in the right of the image seems to be a conglomerate of large and small particles.

Figure 3(b) is approximately 1.12 mm in width. Note that Figure 3(b) is about the same physical size as Figure 3(a), but the large particles have been eliminated by sieving through a 75 μm sieve and many of the smaller particles have been eliminated by sieving through a 20 μm sieve. Note the irregular, non-spherical shapes, typical of a ground rocky material.

Figure 3(c) is approximately 0.16 mm in width. As in the previous panel, the material used to make these images passed the 75 μm sieve and were retained on the 20 μm sieve. Again note the irregular, non-spherical shapes, typical of a ground rocky material. The particle in the left bottom corner (inside circle) is about 16 μm in width, in this cross-section.

In Figure 4, we show four scanning electron microscope (SEM) images of the JSC-1A sample. Figures 4(a) and (c) correspond to the pristine sample, while Figures 4(b) and (d) correspond to the recovered sample from the pump.

The angularity of the shape is a common feature at all sizes. As can be seen, the irregularity is the norm. In general, the

particles also seem somewhat glassy and faceted, as might be expected from ground volcanic material. Another sign of the volcanic origin of the sample can be perceived in the three central particles in Figure 4(c), where traces of enclosed gas bubbles can be seen in the surface of those particles. In Figure 4(a), we can see some very small particles clinging to the larger particle surfaces. It is probable that these small particles are only clinging through electrostatic forces. The particles show very soft and almost featureless surfaces. In Figure 4(b), we show some particles about 15 μm in radius, which is the characteristic size of this sample as presented above. Qualitatively, based on these admittedly small amount of particles, we can affirm that particle shape is roughly invariant with respect to particle size. This has been seen before for crushed natural particles (Garboczi et al. 2012), albeit at a somewhat larger size scale. Figures 4(c) and (d) have a similar magnification, so here we can observe the difference between the pristine and the recovered sample. In Figure 4(c), the very small particles seem to be more abundant than in Figure 4(d), which is consistent with the size distribution r_{eff} values presented in Table 2.

4. Experimental Scattering Matrix

In Figure 5, we present the experimental scattering matrix elements as functions of the scattering angle at three different

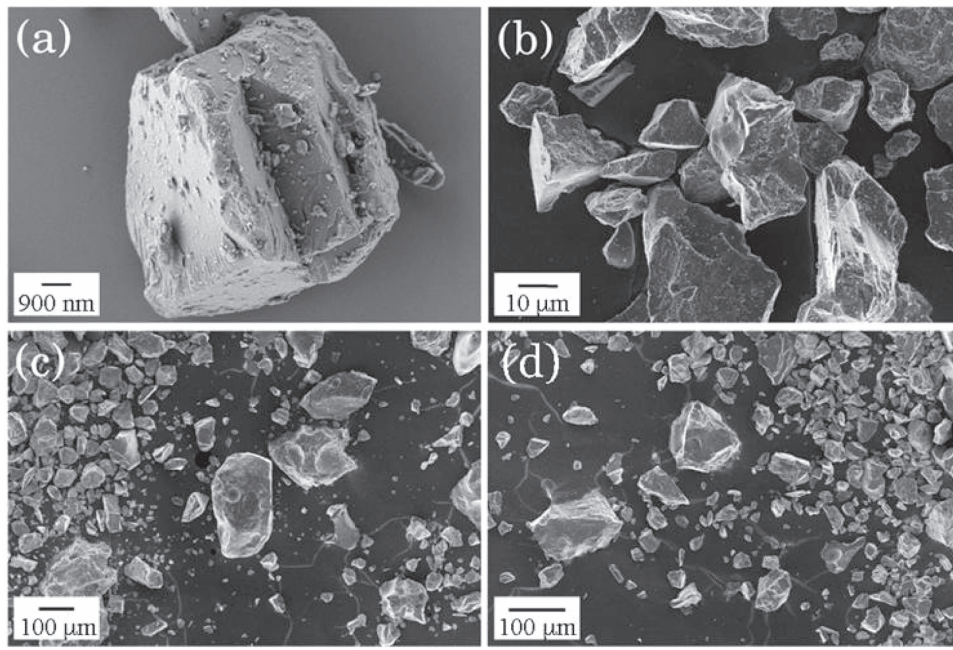


Figure 4. Scanning electron microscope images of the JSC-1A pristine sample and the sample recovered from the jet pump. Panels (a) and (c) correspond to the pristine sample, and panels (b) and (d) correspond to the recovered sample.

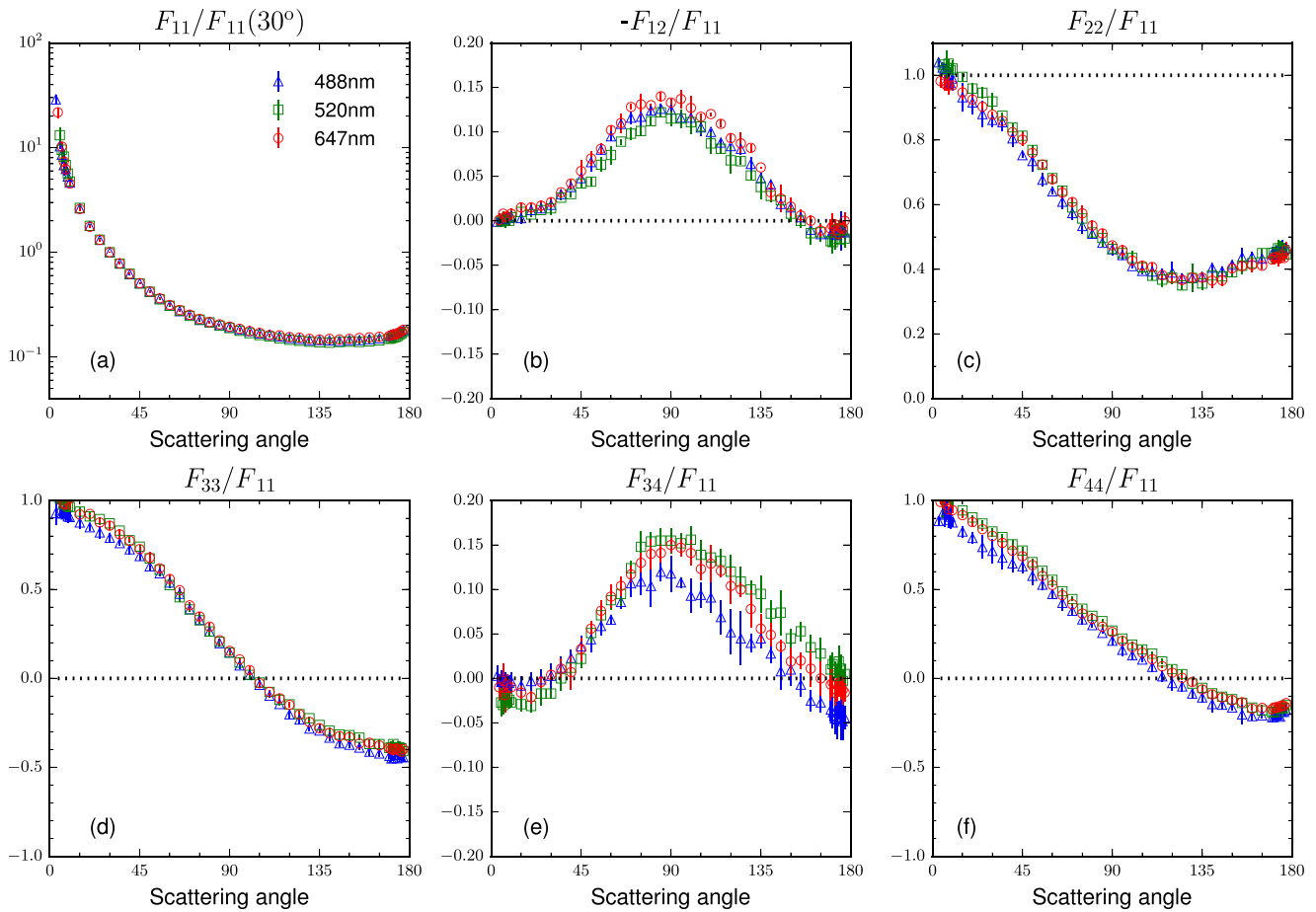


Figure 5. Experimental scattering matrix for lunar simulant JSC-1A at three different wavelengths (488, 520, and 647 nm).

wavelengths (488, 520, and 647 nm). The measurements cover the scattering angle range from 3° to 177° . The ratios $F_{13}(\theta)/F_{11}(\theta)$, $F_{14}(\theta)/F_{11}(\theta)$, $F_{23}(\theta)/F_{11}(\theta)$, and $F_{24}(\theta)/F_{11}(\theta)$

are not represented, since they were found to be zero over the entire angle range within the accuracy of the measurements (as expected by Equation (1)). The experimental errors are

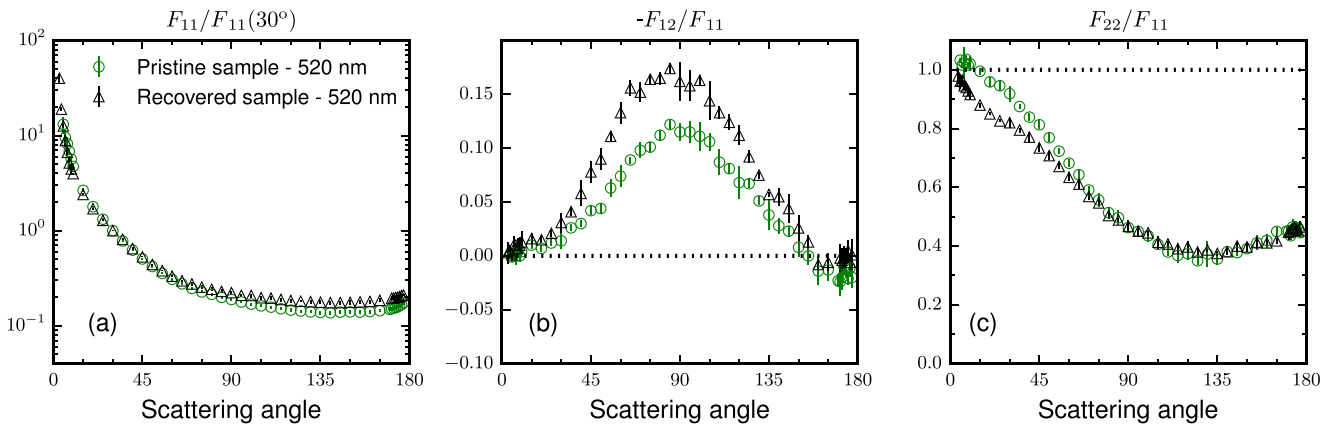


Figure 6. The $F_{11}(\theta)/F_{11}(30^\circ)$, $-F_{12}(\theta)/F_{11}(\theta)$, and $F_{22}(\theta)/F_{11}(\theta)$ experimental scattering ratios for lunar simulant JSC-1A after recovering it once from the pump. The measurements were performed at 520 nm.

represented as error bars (note that some error bars are smaller than the symbol itself). The main source of noise is the statistical variation of the number of large particles passing through the scattering volume, resulting in a smaller signal-to-noise ratio.

The $F_{11}(\theta)/F_{11}(30^\circ)$ ratio, which we have previously defined as the phase function, shows the usual behavior of large irregular mineral dust, i.e., a strong forward peak and almost no structure at side- and back-scattering, as shown in Figure 5(a). The forward diffraction peak can be used to characterize the mean size of the particles as it increases as the particle size grows (Liu et al. 2003). We do not observe any significant difference in the measured values of $F_{11}(\theta)/F_{11}(30^\circ)$ with the wavelength. As stated above, the scattering elements depends mainly on the size, shape, and refractive index of the sample. The lack of differences between wavelengths is indicative of a flat dependence of the imaginary part of the refractive index with the wavelength. Also, the relative size of the wavelength does not significantly change at the measured wavelengths. We have to take into account that some minor differences in the phase function may appear between wavelengths, but the logarithmic representation and the arbitrary normalization to unity at 30 degrees may mask these differences.

The $-F_{12}(\theta)/F_{11}(\theta)$ ratio, shown in Figure 5(b), equals the degree of linear polarization for unpolarized incident light. This plot presents the typical bell shape for irregular particles randomly oriented (Muñoz et al. 2012), with a maximum of polarization near 90° and a small inversion branch at back-scattering ($\sim 2\%$ of negative polarization). The maximum of the degree of linear polarization shows slightly larger values at 647 nm than at 488 nm, i.e., it presents a red polarization color. This has been observed consistently in our database in silicate-type particles when the imaginary part of the refractive index has a constant dependence on the wavelength (see, e.g., Muñoz et al. 2012; Dabrowska et al. 2015).

The $F_{22}(\theta)/F_{11}(\theta)$ ratio, shown in Figure 5(c), is commonly used as a proof of the non-sphericity of the particles, since this ratio equals unity at all scattering angles for optically inactive spheres. The JSC-1A sample shows a $F_{22}(\theta)/F_{11}(\theta)$ ratio different from unity at nearly all measured scattering angles. The depolarization factor (Equation (2)) also depends on this ratio. No significant differences are found between the studied wavelengths.

The $F_{33}(\theta)/F_{11}(\theta)$ and $F_{44}(\theta)/F_{11}(\theta)$ ratios, shown in Figures 5(d) and (f), respectively, can also be studied jointly

as a sign of non-sphericity, indicating irregular particles when they are different from each other (Mishchenko et al. 2000). The measured $F_{44}(\theta)/F_{11}(\theta)$ ratio for the JSC-1A sample is larger than the $F_{33}(\theta)/F_{11}(\theta)$ ratio in the $\sim 75^\circ$ to 177° scattering angle range, while in the case of homogeneous spherical particles the $F_{33}(\theta)/F_{11}(\theta)$ ratio is equal to the $F_{44}(\theta)/F_{11}(\theta)$ ratio at all scattering angles. The $F_{34}(\theta)/F_{11}(\theta)$ ratio, shown in Figure 5(e), shows the strongest wavelength dependence of all measured scattering matrix elements.

We have studied the effect of the loss of small particles on the scattering matrix elements. Due to the limited amount of recycled sample, we have only measured the $F_{11}(\theta)$, $-F_{12}(\theta)/F_{11}(\theta)$ and $F_{22}(\theta)/F_{11}(\theta)$ ratios at 520 nm. In Figure 6, we present the latter scattering elements for the pristine sample and the JSC-1A simulant after one recovery. As stated above, the smaller particles of the sample are depleted during the collecting process. The effect of this depletion on the scattering matrix is noticeable. In the phase function in Figure 6(a), we observe an increase of the forward-scattering peak. This is expected, as this diffraction peak depends on the particle size, being steeper for larger particles. The maximum of the degree of linear polarization increases by a factor of 1.5. Moreover, the maximum is moved toward smaller scattering angles. Apparently, the small particle fraction was determining the maximum of the degree of linear polarization. This is consistent with simulations presented in Liu et al. (2015) for Gaussian random shapes. In those simulations, as the mean size parameter of the particles grows, the resonance scattering region moves into the geometric optics regime, where the maximum in the ratio $-F_{12}(\theta)/F_{11}(\theta)$ increases as the size of the particles increases. Therefore, the small particles are limiting the maximum of the degree of linear polarization. Another interesting feature observed in our results is that the negative polarization branch nearly disappears for the recovered sample. The $F_{22}(\theta)/F_{11}(\theta)$ ratio, shown in Figure 6(c), varies slightly at small scattering angles, but is unaffected at back-scattering, so the depolarization ratio is not altered by the particle recovery process.

4.1. Synthetic Scattering Matrix

As mentioned in Section 2, the laboratory measurements do not cover the whole scattering angle range from 0° to 180° . The lack of measurements at forward and back-scattering angles limits the use of the measured scattering matrix data for

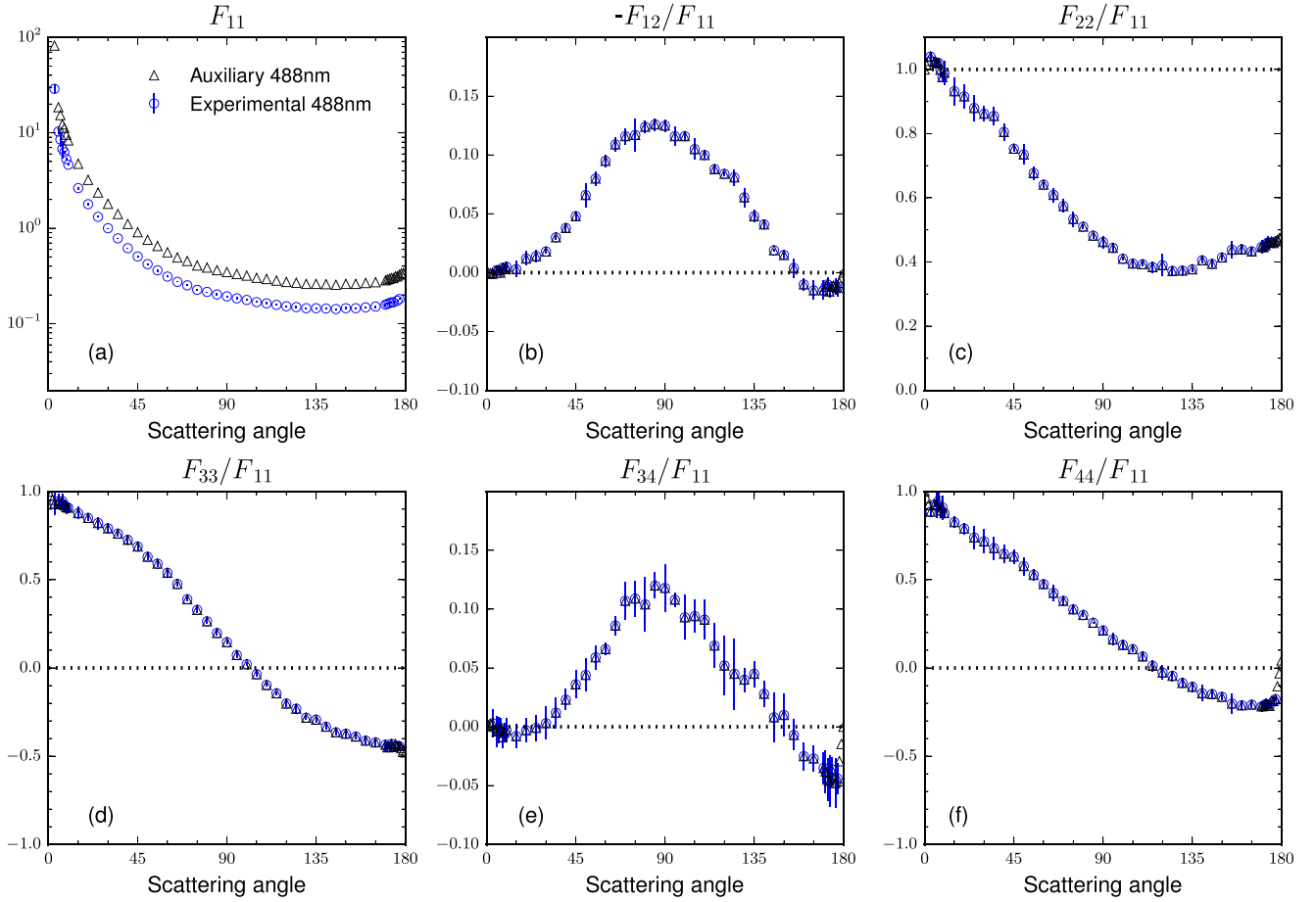


Figure 7. Comparison between the experimental scattering matrix of the JSC-1A lunar simulant at 488 nm (circles) and the extrapolated matrix (triangles). Note that measured $F_{11}(\theta)$ is normalized to unity at 30° , whereas extrapolated $F_{11}^{\text{syn}}(\theta)$ is normalized so that its average over all directions equals unity.

radiative transfer calculations. To facilitate the use of our experimental data we compute the so-called synthetic scattering matrix \mathbf{F}^{syn} from our measurements. This matrix is defined in the full scattering angle range. Therefore, what we measure in the laboratory is the relative phase function $F_{11}(\theta)/F_{11}(30^\circ)$, where (see Volten et al. 2006)

$$\frac{F_{11}(\theta)}{F_{11}(30^\circ)} = \frac{F_{11}^{\text{syn}}(\theta)}{F_{11}^{\text{syn}}(30^\circ)}, \quad (5)$$

and $F_{11}^{\text{syn}}(\theta)$ is the synthetic phase function, which is normalized according to Equation (6):

$$\frac{1}{2} \int_0^\pi d\theta \sin \theta F_{11}^{\text{syn}}(\theta) = 1. \quad (6)$$

The synthetic phase function $F_{11}^{\text{syn}}(\theta)$ covers all the scattering angles from 0° to 180° . The extrapolation of the $F_{11}^{\text{syn}}(\theta)$ element is computed as follows:

1. The forward diffraction peak (0° – 3°) is computed based on the assumption that the forward diffraction peak for randomly oriented particles with moderate aspect ratios mainly depends on the size of the particles and is only weakly dependent of their shape (Liu et al. 2003). We use the Lorenz–Mie theory to compute the scattering produced by projected-surface-area-equivalent spheres between 0° and 3° . These computations depend on the size distribution and the refractive index of the sample.

For the refractive index, we use $m = 1.65 + i0.003$ (Goguen et al. 2010), while the size distributions are those presented in Section 3 (Table 2).

2. Back-scattering extrapolation at 180° is performed using the least squares method for a quadratic function using the measured data from 150° to 177° . As the scattering of randomly oriented irregular particles must be symmetric with respect to the forward and backward directions, the first derivative for all the scattering elements must be null at 0° and 180° (Hovenier & Guirado 2014). The back-scattering is reproduced with a cubic spline interpolation between the last measured data point (177°) and the extrapolated $F_{11}^{\text{syn}}(180^\circ)$ value, taking into account the null derivative condition.
3. At this point, we have a data function given by the measured data from 3° to 177° and extrapolated data from 177° to 180° . This function is shifted vertically until the value of $F_{11}^{\text{syn}}(3^\circ)$, as computed by Lorenz–Mie theory, matches the measured value of $F_{11}(3^\circ)$.

The normalization condition given by Equation (6) is then checked. If it is not satisfied within a 0.1% accuracy, the value of $F_{11}(3^\circ)$ is increased or decreased (within the experimental error bars) depending on whether the integral is greater or smaller than unity, and the three-step process is repeated.

The other missing values of the \mathbf{F}^{syn} matrix elements are interpolated considering the well-known set of constraints of scattering matrices at forward and backward scattering

Table 3

 Asymmetry Parameter g for the JSC-1A Lunar Simulant Retrieved from the Extrapolated Phase Function $F_{11}^{\text{syn}}(\theta)$

Asymmetry Parameter g		
Wavelength λ	Mie	Fraunhofer
488 nm	0.74	0.57
520 nm	0.75	0.60
647 nm	0.74	0.59

Note. The results are presented according to the light-scattering model used in the extrapolation (Mie or Fraunhofer) and depending on the wavelength (488, 520, and 647 nm).

(Hovenier et al. 2004):

$$\frac{F_{12}^{\text{syn}}(0)}{F_{11}^{\text{syn}}(0)} = \frac{F_{12}^{\text{syn}}(180^\circ)}{F_{11}^{\text{syn}}(180^\circ)} = \frac{F_{34}^{\text{syn}}(0)}{F_{11}^{\text{syn}}(0)} = \frac{F_{34}^{\text{syn}}(180^\circ)}{F_{11}^{\text{syn}}(180^\circ)} = 0, \quad (7)$$

$$\frac{F_{22}^{\text{syn}}(0)}{F_{11}^{\text{syn}}(0)} = \frac{F_{33}^{\text{syn}}(0)}{F_{11}^{\text{syn}}(0)} = 1, \quad (8)$$

$$\frac{F_{22}^{\text{syn}}(180^\circ)}{F_{11}^{\text{syn}}(180^\circ)} = -\frac{F_{33}^{\text{syn}}(180^\circ)}{F_{11}^{\text{syn}}(180^\circ)}, \quad (9)$$

$$\frac{F_{44}^{\text{syn}}(180^\circ)}{F_{11}^{\text{syn}}(180^\circ)} = 1 - 2\frac{F_{22}^{\text{syn}}(180^\circ)}{F_{11}^{\text{syn}}(180^\circ)}. \quad (10)$$

Only the value of $F_{22}^{\text{syn}}(180^\circ)/F_{11}^{\text{syn}}(180^\circ)$ must be extrapolated, using the same method as the $F_{11}^{\text{syn}}(180^\circ)$ value explained above. In Figure 7, we present the results of this extrapolation for $\lambda = 488$ nm. Note that measured $F_{11}(\theta)$ is normalized to unity at 30° , whereas extrapolated $F_{11}^{\text{syn}}(\theta)$ is normalized so that its average over all directions equals unity, as stated in Equation (6). Also, the $F_{34}(\theta)/F_{11}(\theta)$ ratio should tend to zero at back-scattering, but there is a gap between the last measured scattering angle and the back-scattering direction. This small disagreement could be due to a slight disadjustment in the V_{DC} during the measurement. Also, we see a step in the $F_{44}(\theta)/F_{11}(\theta)$ ratio. This is probably an artifact of the extrapolation, as this ratio depends on other scattering elements according to Equation (10), so the error inherent to the extrapolations of $F_{11}(180^\circ)$ and $F_{22}(180^\circ)/F_{11}(180^\circ)$ is affecting this result.

The asymmetry parameter g is calculated from the extrapolated phase function using

$$g = \int_0^\pi d\theta \sin \theta \cos \theta F_{11}^{\text{syn}}(\theta). \quad (11)$$

The values of g are presented in Table 3. They are classified depending on the size distribution model used in the extrapolation of $F_{11}^{\text{syn}}(\theta)$ (Mie or Fraunhofer) and for the three visible wavelengths used.

In Table 4, we present the computed depolarization factor $\delta_L(180^\circ)$ using Equation (2). The results are classified according to the wavelength and the light-scattering model used in the extrapolation.

5. Conclusions

We presented the 4×4 experimental scattering matrices for the lunar simulant JSC-1A at three visible wavelengths (488, 520, and 647 nm). The data were extrapolated at forward- and back-scattering to obtain the synthetic matrices that cover the

Table 4

 Back-scattering Depolarization Factor $\delta_L(180^\circ)$ for the JSC-1A Lunar Simulant Retrieved from Equation (2) and the Extrapolated $F_{22}^{\text{syn}}(180^\circ)$

Back-scattering Depolarization Factor $\delta_L(180^\circ)$		
Wavelength λ	Mie	Fraunhofer
488 nm	0.35	0.35
520 nm	0.42	0.42
647 nm	0.31	0.31

Note. The results are presented according to the light-scattering model used in the extrapolation (Mie or Fraunhofer) and depending on the wavelength (488, 520, and 647 nm).

whole scattering range from 0° to 180° . The size distribution of the sample was also measured for the pristine sample and after being recovered twice from the collecting device to study the size-selection effect. Tables of the measured and synthetic scattering matrices are available in the Amsterdam–Granada Light Scattering Database (www.iaa.es/scattering). The data are freely available pending a citation of this paper and Muñoz et al. (2012).

In general, the experimental matrices were very similar at all the studied wavelengths. The results show a behavior typical for mineral dust. The $-F_{12}(\theta)/F_{11}(\theta)$ ratio shows a red polarization color. This seems to indicate a nearly constant value of the imaginary part of the refractive index at the measured wavelengths (see, e.g., Muñoz et al. 2012; Dabrowska et al. 2015).





The measured data were extrapolated at forward- and back-scattering, and the asymmetry parameter g and back-scattering linear depolarization factor δ_L were computed from this synthetic matrices. The retrieved linear depolarization ratio varies with wavelength, obtaining values of 0.35, 0.42, and 0.31 at 488 nm, 520 nm, and 647 nm, respectively.

The effect of removing particles smaller than $1 \mu\text{m}$ in radius on the measured $F_{11}(\theta)$, $-F_{12}(\theta)/F_{11}(\theta)$, and $F_{22}(\theta)/F_{11}(\theta)$ ratios was studied. As the small particles were depleted from the sample due to the filters in the pump system, the forward-scattering peak of the phase function became steeper. Furthermore, the maximum of the degree of linear polarization maximum increased, moving toward smaller scattering angles. The negative polarization branch at large scattering angles nearly disappeared after removing the sub-micron fraction from the sample. The $F_{22}(\theta)/F_{11}(\theta)$ ratio was slightly affected in the forward direction and unaffected in back-scattering.

For future work, it would be interesting to study highland simulants like the MLS-1 (Weiblen et al. 1990) to compare with the results presented here. The final step for these studies would be to measure the scattering matrix of a lunar regolith sample to verify the suitability of these simulants as optopolarimetric replicas of the Moon surface's dust.

The contributions of co-authors J.D. Goguen and R.A. West were carried out at the Jet Propulsion Laboratory, California Institute of Technology, under a contract with the National Aeronautics and Space Administration. We are indebted to Rocío Márquez from the Scientific Instrumentation center of the University of Granada for providing part of the SEM images. This work has been supported by the Plan Nacional de Astronomía y Astrofísica contracts AYA2015-67152-R and AYA2015-71975-REDT.

ORCID iDs

J. Escobar-Cerezo  <https://orcid.org/0000-0003-0432-4443>
 O. Muñoz  <https://orcid.org/0000-0002-5138-3932>
 F. Moreno  <https://orcid.org/0000-0003-0670-356X>
 J. C. Gómez Martín  <https://orcid.org/0000-0001-7972-085X>

References

- Dabrowska, D. D., Muñoz, O., Moreno, F., et al. 2015, *Icar*, **250**, 83
 Garboczi, E. J. 2011, *Powder Technology*, 207, 96
 Garboczi, E. J., Liu, X., & Taylor, M. A. 2012, *Powder Technology*, 229, 84
 Goguen, J. D., Stone, T. C., Kieffer, H. H., & Buratti, B. J. 2010, *Icar*, **208**, 548
 Hansen, J. E., & Travis, L. D. 1974, *SSRv*, **16**, 527
 Hovenier, J. W., & Guirado, D. 2014, *JQSRT*, **133**, 596
 Hovenier, J. W., van de Hulst, H. C., & van der Mee, C. V. M. 1986, *A&A*, **157**, 301
 Hovenier, J. W., Van Der Mee, C., & Domke, H. 2004, *Transfer of Polarized Light in Planetary Atmospheres: Basic Concepts and Practical Methods*, Vol. 318 (Dordrecht: Kluwer)
 Liu, J., Yang, P., & Muinonen, K. 2015, *JQSRT*, **161**, 136
 Liu, L., Mishchenko, M. I., Hovenier, J. W., Volten, H., & Muñoz, O. 2003, *JQSRT*, **79**, 911
 Lyot, B. 1929, *Annales de l'Observatoire de Paris, section de Meudon*, 8, 1
 McKay, D. S., Carter, J. L., Boles, W. W., Allen, C. C., & Alton, J. H. 1994, in *Engineering, Construction, and Operations in Space IV*, ed. R. G. Galloway & S. Lokaj (New York: American Society of Civil Engineers), 857
 Mie, G. 1908, *AnP*, **330**, 377
 Mishchenko, M. I., Travis, L. D., & Lacis, A. A. 2002, *Scattering, Absorption, and Emission of Light by Small Particles* (Cambridge: Cambridge Univ. Press)
 Mishchenko, M. I., Wiscombe, W. J., Hovenier, J. W., & Travis, L. D. 2000, in *Light Scattering by Nonspherical Particles: Theory, Measurements, and Applications*, ed. M. I. Mishchenko, J. W. Hovenier, & L. D. Travis (New York: Academic), 30
 Muñoz, O., Moreno, F., Guirado, D., et al. 2010, *JQSRT*, **111**, 187
 Muñoz, O., Moreno, F., Guirado, D., et al. 2011, *Icar*, **211**, 894
 Muñoz, O., Moreno, F., Guirado, D., et al. 2012, *JQSRT*, **113**, 565
 Muñoz, O., Volten, H., Hovenier, J. W., et al. 2006, *A&A*, **446**, 525
 Papike, J. J., Simon, S. B., & Lul, J. C. 1982, *RvGSP*, **20**, 761
 Ray, C. S., Reis, S. T., Sen, S., & O'Dell, J. S. 2010, *JNCS*, **356**, 2369
 Sterzik, M. F., Bagnulo, S., & Palle, E. 2012, *Natur*, **483**, 64
 van de Hulst, H. C. 1957, *Light Scattering by Small Particles* (New York: Wiley)
 Volten, H., Muñoz, O., Hovenier, J. W., & Waters, L. B. F. M. 2006, *JQSRT*, **100**, 437
 Weiblen, P. W., Murawa, M. J., & Reid, K. J. 1990, in *Engineering, Construction and Operations in Space II, Preparation of Simulants for Lunar Surface Materials*, ed. S. W. Johnson (New York: American Society of Civil Engineers), 428